Available online at www.sciencedirect.com
SCIENCE DIRECT
Catalysis Today 114 (2006) 142–153
CATALYSIS TODAY
www.elsevier.com/locate/cattod

States of transition metal ions in modified mesoporous MCM-41 and in microporous ZSM-5 studied by ESR spectroscopy

Piotr Decyk

Faculty of Chemistry, A. Mickiewicz University, Grunwaldzka 6, 60-780 Poznań, Poland

Available online 17 February 2006

Abstract

This paper reviews a series of studies published recently on silicate, aluminosilicate, and niobosilicate micro- and mesoporous molecular sieves modified with transition metals (Cu, Fe, V). These metals were incorporated during the synthesis or in the post-synthesis procedures (impregnation, ion exchange, chemical vapour deposition, immobilisation of organic complex). In case of niobosilicate matrix, the strong interaction between the included metal and niobium species was detected by electron spin resonance spectroscopy (ESR) investigation. The reducibility of metal species in relation to the structure and composition of matrix is discussed. The results of the adsorption of probe molecules (NO, CO, SO_2) are shown and discussed.

Keywords: ZSM-5 and MCM-41 materials; Cu^{2+}; Fe^{3+} and V^{4+} paramagnetic cations; Paramagnetic species; ESR spectroscopy

1. Introduction

A lot of redox catalytic processes proceed via radical reaction pathways. Therefore, the detailed study of radical species formed on the catalyst surface is of a great interest for the estimation of reaction mechanisms. One can consider metal paramagnetic centres, metal–oxygen complexes, and oxygen radicals as important species in catalysis.

Some important review papers concerning the state of transition metal ions in the materials, potential catalysts, have already been published [1–9]. These papers widely describe various techniques, including ESR, applied for the study of bulk transition metal oxides and oxides supported on various solids. The aim of this paper is to show the effectiveness of the use of ESR study for the estimation of the state of transition metals located in the micro- and mesoporous matrices.

Two kinds of materials often used as supports for paramagnetic species are microporous molecular sieves (zeolites) and mesoporous molecular sieve (MCM-41 most often studied).

There is a significant difference in the structure of zeolites and mesoporous molecular sieves. First of all microporous zeolites are strictly crystalline with three dimensional translation symmetry, whereas mesoporous MCM-41 in fact are amorphous. The latter are built from hexagonally ordered mesopores surrounded by amorphous silica or metalosilicates. The crystallinity of MCM-41 molecular sieves is related to the well hexagonally ordered mesopores giving rise to the apperance of XRD signals at $2\Theta < 7$ degree region. The thickness of amorphous walls in MCM-41 varies depending on the preparation methods and metal element introduced during the synthesis together with silicon. In a consequence, metals introduced via cation exchange procedure can be relatively easily incorporated into the walls of MCM-41 and therefore can occupy both framework and extra framework positions. The distinction between both locations is not clear contrary to ZSM-5 zeolites. The different localisation of transition metal in MCM-41 (in both, extra framework and framework positions) and ZSM-5 (only in the extra framework sites) leads to various microenvironment of metal species which determines the surface behaviour. Therefore, one can expect that the structural differences between ZSM-5 and MCM-41 materials will result in various surface and catalytic properties of transition metals modifying micro- and mesoporous molecular sieves. This behaviour is well illustrated by Stockenhuber et al. [10–12]. The authors stated that the main difference between FeZSM-5 and FeMCM-41 materials is the presence of Fe–O nanoclusters in FeZSM-5 which seem to be more active in the oxidation reaction than isolated irons entities in mesoporous molecular sieves [12].

E-mail address: piotrd@amu.edu.pl.

0920-5861/$ – see front matter © 2006 Elsevier B.V. All rights reserved.
doi:10.1016/j.cattod.2006.01.013

This paper reviews the results reported earlier [13–27] and adds some new data which allow the presentation of new insight into paramagnetic species formed on iron, copper, vanadium, and niobium containing molecular sieves (micro- and mesoporous) studied by ESR.

2. Experimental

2.1. Preparation

For the preparation of MCM-41 and TMCM-41 (T: Al, Nb, V) materials, the classical hydrothermal synthesis in the polypropylene bottles has been used [28]. The synthesis at room temperature was applied for CuAlMCM-41 and CuNbMCM-41 preparation. In both syntheses routes *n*-hexadecyltrimethylammonium chloride (Aldrich), was used as a surfactant; sodium silicate (Aldrich), aluminium sulphate (POCH, Poland), niobium(V)oxalate (CBMM-Brasil), niobium(V) chloride (Aldrich), vanadyl(IV) sulphate (BDH) were precursors of Si, Al, and V, respectively. For preparation of Cu containing catalysts, tetraethoxysilane (TEOS) (Aldrich), and copper(II) acetate (POCH, Poland) were precursors of Si and copper.

The parent materials used for the post-synthesis modification with iron and copper, were AlZSM-5, and NbZSM-5 zeolites, and MCM-41, AlMCM-41 and NbMCM-41 molecular sieves.

2.2. Sample identification

The samples used and summary of their preparation methods are presented in Tables 1–4. The explanation of symbols used in this work for MCM-41 type materials is as follows:

- The number after ‘‘41’’ denotes Si/T assumed ratio (T, metal other than Si) (example: CuAlMCM-41-32, Si/Al = 32).

Table 1
The copper samples described in this work and summary of the preparation procedures

Sample	Preparation procedure	
CuAlMCM-41-32 CuNbMCM-41-32	Synthesis at RT [24]	Synthesis
Cu-AlMCM-41-64-150 Cu-AlMCM-41-32-132 Cu-AlMCM-41-16-97 Cu-NbMCM-41-32-112	Ion exchange from aqueous solution of $Cu(CH_3COO)_2$, after filtration the solid was dried at 393 K and calcined at 673 K for 4 h [15]	Post-synthesis
Cu-AlZSM-5-31-96 Cu-NbZSM-5-28-106	Ion exchange from aqueous solution of $Cu(CH_3COO)_2$, after filtration the solid was dried at 393 K and calcined at 673 K for 4 h [22]	Post-synthesis

Table 2
Iron containing samples and summary of the preparation procedures

Sample	Preparation procedure
Fe-ZSM-5 (IE)	Ion exchange (IE) from aqueous solution of $Fe(NO_3)_3$, after filtration and washing the solid was dried at 393 K and calcined at 773 K [21]
Fe-MCM-41 (TIE) Fe-AlMCM-41-32 (TIE)	Template ion exchange (TIE)—done like ion exchange, but without template removal before the procedure [21]
Fe-ZSM-5 (CVD)	Chemical vapour deposition (CVD)—$FeCl_3$ was sublimed at 603 K for 3 h, next the sample was calcined at 823 K for 4 h [19]
Fe(FAA)/MCM-41 Fe(FAA)/AlMCM-41-32 Fe(FAA)/AlMCM-41-128	Immobilisation of ferrocenoacetic acid (FAA) was performed by immersing and mixing the solid in toluene solution for 3 h and drying at 353 K for 10 h next calcined at 773 K for 5 h [27]

Table 3
Niobium containing samples and summary of the preparation procedures

Sample	Preparation procedure
Nb(Cl)MCM-41-32 Nb(O)MCM-41-32 Nb(O)MCM-41-16	Hydrothermal synthesis; assumed ratio of Si/Nb = 32 or 16 (the last number in the symbols denotes this ratio), Nb-source/preparation: (O)-Nb(V) oxalate, (Cl)-Nb(V) chloride [20]

- Slash indicates the impregnation method applied (example: Fe(FAA)/MCM-41 means impregnation of MCM-41 with ferroceneacetic acid leading to Fe species after calcination).
- ‘‘-’’ between metal and the symbol of parent molecular sieve stands by ion exchange method (example: Cu-NbMCM-41-32-112). The last number is such catalysts shows the percent of cation exchanged taking to account one Cu^{2+} exchanges two Na^+. The numbers above 100 indicates that a part of metal occupies noncationic positions.
- The letters in brackets at the end of the catalyst symbols described the type of post-synthesis procedure, namely: (IE)—ion exchange; (TIE)—template ion exchange; (CVD)—chemical vapour deposition (example: Fe-MCM-41(TIE)).

2.3. Characterisation

The following techniques were used for the samples characterisation. The XRD and N_2 adsorption were applied for texture/structure characterisation. XRD patterns were obtained on TUR 42 diffractometer with Cu Kα radiation. The surface area and pore volume of the MCM-41 materials

Table 4
Vanadium containing samples and summary of the preparation procedures

Sample	Preparation procedure
VMCM-41-32 VMCM-41-128	Hydrothermal synthesis; assumed ratio of Si/V = 32 or 128, (the last number in the symbols denotes this ratio) [25]
VNbMCM-41-51	[26]

Table 5
Composition of copper containing microporous materials [22]

Sample	Si/T[a]	Cu/T[a]	Cu (wt.%)	Cu (ex.%)
Cu-AlZSM-5-96	31	0.48	1.6	96
Cu-NbZSM-5-106	28	0.53	1.9	106

[a] T: Al or Nb in the lattice.

were measured by nitrogen adsorption at 77 K using the conventional technique on a Micromeritics 2010 apparatus. The ESR spectra were recorded at 77 K and RT on a RADIOPAN SE/X 2547 spectrometer. A cavity operating at a frequency of 8.9 GHz (X-band) was used.

2.3.1. Copper containing samples

2.3.1.1. Role of texture/structure of matrix. The composition of copper containing samples and their textural/structural parameters are listed in Tables 5 and 6. All the prepared copper containing MCM-41 are mesoporous materials with high surface areas and pore volumes. Both parameters drastically decrease in Cu-NbMCM-41-32-112 suggesting the formation of some aggregates in the pores. The other part of modified materials exhibits only slightly lower values of surface area and pore volume in comparison to those of parent samples.

The behaviour of Cu^{2+} cation ($3d^9$, $^2D_{5/2}$) and its complexes on solid surfaces, is one of the most studied subjects, since its ESR spectra can be observed easily and are affected significantly by the environment. The ESR studies allow the estimation of the sitting-coordination of cupric cations in molecular sieves, the Cu^{2+} reduction degree during the activation and the paramagnetic complexes formed after NO adsorption, i.e., Cu^{+}(NO) and/or $Cu^{2+}O^{-}$(NO) [29–34].

The cupric ion sitting-coordination in CuZSM-5 zeolites is well defined and described in the literature [35–38]. There are: (i) octahedral ($g_{||} = 2.38$, $A_{||} = 100$–140 G), (ii) square pyramidal ($g_{||} = 2.33$, $A_{||} = 140$–160 G), and (iii) square planar ($g_{||} = 2.27$, $A_{||} = 170$–180 G). The distribution of these sites in the zeolite matrix depends on the Cu loading, Si/Al ratio and water content in the sample. The thermal treatment of zeolites, Cu-AlZSM-5-96 and Cu-NbZSM-5-106, under vacuum at increasing temperatures leads to the progressive appearance of various Cu^{2+} species. Moreover, in parallel, a decrease in the signal intensity indicates a partial reduction of Cu^{2+} [14,15,22]. A comparison of the ESR signal intensity drops caused by the increase of the evacuation temperature of Cu-AlZSM-5-96 versus the signal intensity drops of Cu-NbZSM-5–106 reported in [22], indicates that autoreduction of Cu^{2+} occurs slightly more easily on an aluminosilica than on a niobiosilica matrix.

The ESR parameters presented in Table 7 reveal a transformation of octahedrally coordinated Cu^{2+}, liganded by molecules of water [3,37–39], ($g_{||} = 2.38$, $A_{||} = 137$ G for Cu-AlZSM-5-96) and ($g_{||} = 2.37$, $A_{||} = 135$ G for Cu-NbZSM-5-106), present in the fresh sample and the materials evacuated at RT. The transformation of Cu-octahedral into Cu-square pyramidal structures in which copper is coordinated with oxygen [40], for Cu-AlZSM-5 occurs at 373 K (during the evacuation), whereas on Cu-NbZSM-5 it takes place at 573 K. The next transformation to a square planar structure is only slightly observed on Cu-NbZSM-5 after evacuation at 723 K and is very well visible on Cu-AlZSM-5 evacuated at 473 K. The values (Table 7) are lower when the Nb-containing matrix is applied. It is worthy of notice that the considered changes in Cu coordination correspond only to residual ESR-visible cations. One cannot exclude the possibility that a part of the ESR silent Cu^{2+} transforms also to square planar structures and cannot be observed [22].

The Cu-modified mesoporous molecular sieves evacuated at the increasing temperatures do not show Cu^{2+} ions in a square planar structure (Table 8). This kind of divalent Cu cations, which are easily reduced and prevails in population at high Cu loading, is described as the Cu site active in NO decomposition [41,42,43]. In the samples with various Si/Al ratios and the Cu exchange level $\geq 100\%$, the evacuation at 723 K leads to the reduction of ca. 70% of cupric ions (i.e., less than in Cu-AlZSM-5-96). The lower degree of a copper exchange causes a complete reduction of cupric cations when evacuated at 673 K (the ESR signal disappears). The activity of this sample in the NO decomposition is extremely low [15].

2.3.1.2. Role of the T element in the lattice. The autoreduction of copper in the MFI and MCM-41 matrices during evacuation or activation in the flow of an inert gas strongly depends on a nature of the T-element in the framework. A slightly lower number of Cu^{2+} cations is reduced at the same conditions on Cu-NbZSM-5 than on Cu-AlZSM-5 as shown from the ESR results [22]. However, the reduction of copper in the Nb containing matrix is deeper than that in the aluminosilica zeolite which was confirmed from ESR study after adsorption of NO (see more details in Section 2.3.1.3). Moreover, the ESR signal from the paramagnetic copper almost completely disappears after evacuation of CuNbMCM-41-32-112 at 723 K, whereas it is preserved (with a lower intensity)

Table 6
The characteristic of copper containing mesoporous materials [18,24]

Sample	Cu (wt.%)	Si/Me[a] assumed	Surface area (m^2/g) BET	Mesopore volume (cm^3/g), BJH-des	Pore diameter (nm)
CuAlMCM-41-32 (RT) synt	1.1	32	1100	0.9	3.3
CuNbMCM-41-32 (RT) synt	0.9	32	1100	0.8	3.3
Cu-AlMCM-41-64-150	1.2	64	913	1.3	2.2
Cu-AlMCM-41-32-132	2.1	32	925	1.3	2.3
Cu-NbMCM-41-32-112	1.9	32	839	0.6	1.5

[a] Me: Al or Nb in the lattice.

Table 7
ESR parameters determined for the Cu containing ZSM-5 zeolites [22]

Sample	Treatment	Octahedral		Square pyramidal		Square planar	
		$g_{\|\|}$	$A_{\|\|}$ (G)	$g_{\|\|}$	$A_{\|\|}$ (G)	$g_{\|\|}$	$A_{\|\|}$ (G)
Cu-AlZSM-5-96	Fresh	2.38	137				
	Evacuated at RT	2.38	137				
	Evacuated at 373 K			2.34	156		
	Evacuated at 473 K			2.32	143	2.28	168
	Evacuated at 723 K			2.32	143	2.27	169
	Adsorption of NO			2.32	144	2.28	169
Cu-NbZSM-5-106	Fresh	2.37	135				
	Evacuated at RT	2.37	135				
	Evacuated at 373 K	2.37	136				
	Evacuated at 473 K	2.37	133				
	Evacuated at 573 K			2.34	134		
	Evacuated at 673 K			2.34	131		
	Evacuated at 723 K			2.34	140	2.28	162
	Adsorption of NO			2.34	148		

after treatment of CuAlMCM-41-32-132 under the same conditions [17].

2.3.1.3. ESR study on ZSM-5 and MCM-41 materials after adsorption of NO. The adsorption of NO at RT on Cu-AlZSM-5 leads to the formation of well known, from the literature, paramagnetic Cu^{+}(NO) complex [29,32–34] and to the oxidation of copper to Cu^{2+}. The increase in the ESR signal intensity (Fig. 1A, spectrum b) is observed. This means that the sample evacuated at 723 K has Cu^{+} ions and that copper reduced species is easily oxidized by NO. The effect of NO adsorption on Cu-NbZSM-5 (Fig. 1B) is the same concerning copper oxidation. The comparison of spectra a and c (Fig. 1B) indicates that NO adsorption is a reversible process. The ESR signal (Fig. 1B spectrum d) formed is not typical of Cu^{+}(NO) but can be assigned to the $Cu^{2+}O^{-}$(NO) paramagnetic complex [30] or to the other $Cu^{\delta+}$(NO) species. There is no signal due to the Cu^{+}(NO) complex, as on Cu-AlZSM-5 zeolite, and the IR study evidenced that copper is more metallic than Cu^{+}, i.e., it is $Cu^{\delta+}$ ($\delta < 1$) [22]. The reduction of Cu^{2+} to $Cu^{\delta+}$ was confirmed also with FTIR study followed by NO adsorption [22]. Moreover, Cu^{2+}–ligand interaction is stronger in Cu-NbZSM-5 than in Cu-AlZSM-5, which makes transformation from octahedral to square pyramidal and square planar structures more difficult in Nb-containing molecular sieves (Table 7).

The presence of Cu^{+} cations in evacuated Cu-AlMCM-41 is documented by the formation of Cu^{+}(NO) complex after NO adsorption. Such Cu^{+}(NO) complex is well visible in the ESR spectra of NO adsorbed on Cu-AlMCM-41-16-97 and Cu-AlMCM-41-32-132 but not on Cu-AlMCM-41-64-150. Similar

Table 8
ESR parameters determined for the Cu-containing AlMCM-41 samples [15]

Sample	Treatment	Octahedral		Square pyramidal		Square planar	
		$g_{\|\|}$	$A_{\|\|}$ (G)	$g_{\|\|}$	$A_{\|\|}$ (G)	$g_{\|\|}$	$A_{\|\|}$ (G)
CuAlMCM-41-64-150	Fresh	2.38	136				
	Evacuated at RT	2.37	138				
	Evacuated at 373 K			2.33	161		
	Evacuated at 473 K			2.32	161		
	Evacuated at 723 K			2.32	160		
	Adsorption of NO			2.32	163		
CuAlMCM-41-32-132	Fresh	2.38	136				
	Evacuated at RT	2.37	138				
	Evacuated at 373 K			2.32	168		
	Evacuated at 473 K			2.31	164		
	Evacuated at 723 K			2.31	162		
	Adsorption of NO			2.31	163		
CuAlMCM-41-16-97	Fresh						
	Evacuated at RT						
	Evacuated at 373 K						
	Evacuated at 473 K			2.31	162		
	Evacuated at 723 K			2.31	164		
	Adsorption of NO			2.30	166		

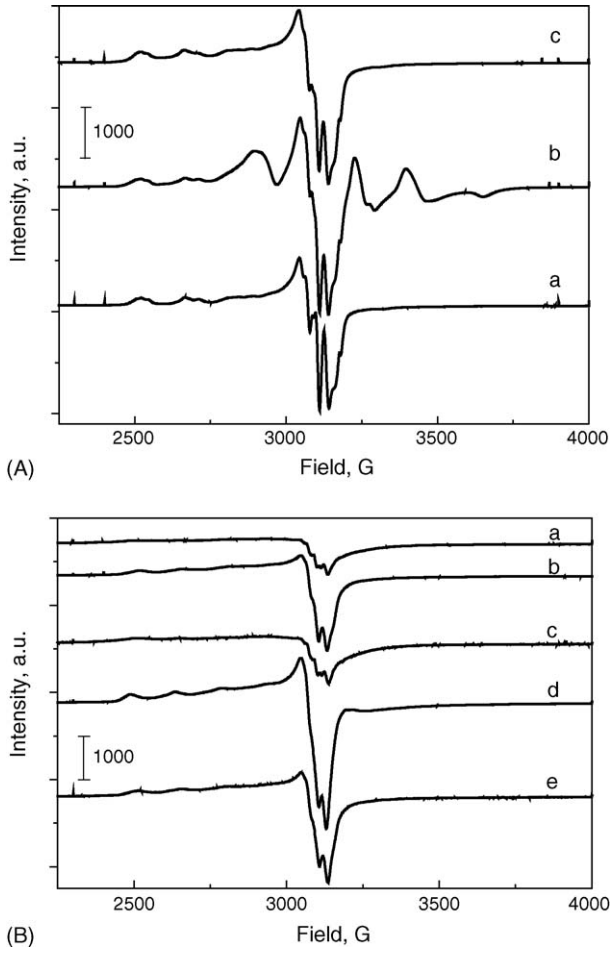

Fig. 1. Effect of NO adsorption—ESR spectra recorded at 77 K. Cu-AlZSM-5-96 (A): after evacuation at 723 K (a), after NO adsorption at RT (b), and followed by evacuation at 473 K (c). Cu-NbZSM-5-106 (B): after evacuation at 723 K (a), after NO adsorption at RT and evacuation at RT (b), followed by evacuation at 723 K (c), after next adsorption of NO (d), and after evacuation at RT (e) [22].

as in Cu-AlZSM-5, NO adsorption on Cu-AlMCM-41-32-132 leads to the generation of $Cu^{+}(NO)$ complex which almost disappears after admission of a higher amount of NO. It suggests the formation of ESR silent dinitrosyl species, $Cu(NO)_2$. The appearance of the $Cu^{+}(NO)$ complex after NO adsorption is accompanied by a slight growth in the Cu^{2+} signal intensity indicating a partial oxidation of Cu^{+} to Cu^{2+} [15,44].

The evacuation at 723 K of the sample with Si/Al = 64 followed by NO adsorption gives rise to the appearance of a weak ESR signal. It does not origin from $Cu^{+}(NO)$ demonstrated in Fig. 1A. It could be assigned to $Cu^{2+}O^{-}(NO)$ species which is observable in the ESR spectra [30] and can be formed after NO adsorption on $Cu^{2+}O^{-}$, generated during an autoreduction of $(Cu^{2+}OH^{-})^{+}$ existing in the extra framework position of a fresh sample [15,30]. The NO adsorption at RT on Cu-NbMCM-41-32-112 sample evacuated at 723 K causes a partial oxidation of the reduced copper species evidenced by an appearance of the ESR signal (the hyperfine structure) due to Cu^{2+} cations besides the signal from the $Cu^{+}NO$ complex [17]. When Nb-containing mesoporous matrix is applied, copper is more easily reduced than if Cu is introduced into the AlMCM-41 material. A negative charge located on $Nb–O^{-}$ in the skeleton of the mesoporous material makes the copper reduction easier [17]. The $Nb–O^{-}$ exhibits an ion radical character and this kind of species will be discussed below.

2.3.1.4. ESR investigation of MCM-41 materials with copper incorporated into the framework. The ESR spectra of CuAlMCM-41-32 and CuNbMCM-41-32 (Cu incorporated during the synthesis) provide the information about coordination of copper after various vacuum treatments [24]. Table 9 shows g and A factors calculated from the spectra obtained after evacuation of the samples studied at various temperatures. The decrease of the ESR signal intensity of CuAlMCM-41-32 material (not shown here) with the growth of evacuation temperature to 473 K is caused mainly by the dehydratation process. The higher evacuation temperature leads to the further decrease of the ESR signal intensity indicating autoreduction of Cu^{2+} to Cu^{+}. Table 9 shows three types of structures for copper species. Type I characterised by $g = 2.37–2.38$ and $A = 135–138$ G is assigned to octahedrally coordinated copper liganded by water molecules [3,37–39,43]. The existence of such species suggests that at least a part of copper is localised in the extra framework position where it exists as hexa–aqua-complex at RT. Two hours evacuation at RT causes the transformation of octahedrally coordinated copper into square pyramidal structure ($g = 2.31$, $A = 169$ G)-II type—in which Cu is coordinated with oxygen [40]. Such transformation in Cu-exchanged material occurs at higher temperature (373 K). In CuAlMCM-41–32 (Cu incorporated during the synthesis) evacuation at 373 K leads to the appearance of the third kind of Cu-species ($g = 2.29$, $A = 164$ G), which was not observed in Cu-exchanged material. The g and A parameters of this species are close to that ascribed in the literature [45–47] to Cu in square planar structure.The behaviour of CuNbMCM-41-32 materials is different and is estimated from ESR spectra (Fig. 2) and data in Table 9. In contrast to the case of CuAlMCM-41-32, octahedrally coordinated Cu species does not appear in the respective sample. The fresh CuNbMCM-41-32 sample exhibits copper species of type II, it means cations coordinated to oxygen. According to the literature [48,49], the g and A parameters for fresh CuNbMCM-41-32 shown in Table 9 indicates the four-coordinated complex with tetrahedrally distorted square symmetry. A similar species has been detected previously (Table 9) for Cu exchanged NbMCM-41 material (Cu-NbMCM-41-32-112) but after evacuation at 373 K. However, in the case of CuNbMCM-41-32 (Cu included during the synthesis) the evacuation of the material with the increasing temperature causes the hyperfine structure to diminish contrary to the behaviour of Cu-exchanged material. Finally, the evacuation at 473 K significantly changes the behaviour of ESR spectrum (Fig. 2). The hyperfine structure is not resolved. A much broader ESR line appears. Similar feature was observed by Munoz et al. [50] for CuAPO-5 dehydrated at 723 K. The authors did not define the Cu structure giving this kind of ESR signal. However, they concluded the presence of tetrahedrally coordinated copper in the molecular sieve CuAPO-5. Taking that into account one can suppose, that in

Table 9
ESR parameters determined for Cu-containing NbMCM-41 and AlMCM-41 materials [24]

Sample	Pretreatment	Coordination					
		Type I		Type II		Others	
		$g_{\|\|}$	$A_{\|\|}$ (G)	$g_{\|\|}$	$A_{\|\|}$ (G)	$g_{\|\|}$	$A_{\|\|}$ (G)
CuAlMCM-41-32	Fresh	2.37	135				
(synthesised)	Evacuated at RT			2.31	169		
	Evacuated at 373 K			2.32	159	2.29	164
	Evacuated at 473 K			2.32	162	2.29	164
	Evacuated at 723 K			2.31	164		
CuAlMCM-41-32w	Fresh	2.38	136				
(synthesised)	Evacuated at RT	2.38	136				
	Evacuated at 373 K			2.34	156		
	Evacuated at 473 K			2.32	164		
Cu-NbMCM-41-32-112	Fresh	2.39	133				
(cation-exchanged) [18]	Evacuated at RT	2.38	133				
	Evacuated at 373 K			2.34	139		
	Evacuated at 473 K			2.33	142		
	Evacuated at 723 K			2.30	168		
CuNbMCM-41-32	Fresh			2.34	138		
(synthesised)	Evacuated at RT			2.30	157		
CuNbMCM-41-32w	Fresh	2.37	134				
(synthesised)	Evacuated at RT			2.35	131		

w: samples after stirring with water.

the presented study the use of Cu together with Nb in the gel applied for the synthesis leads to the location of copper in the different position than that in Cu-exchanged materials (presumably partially in the skeleton of MCM-41 material).

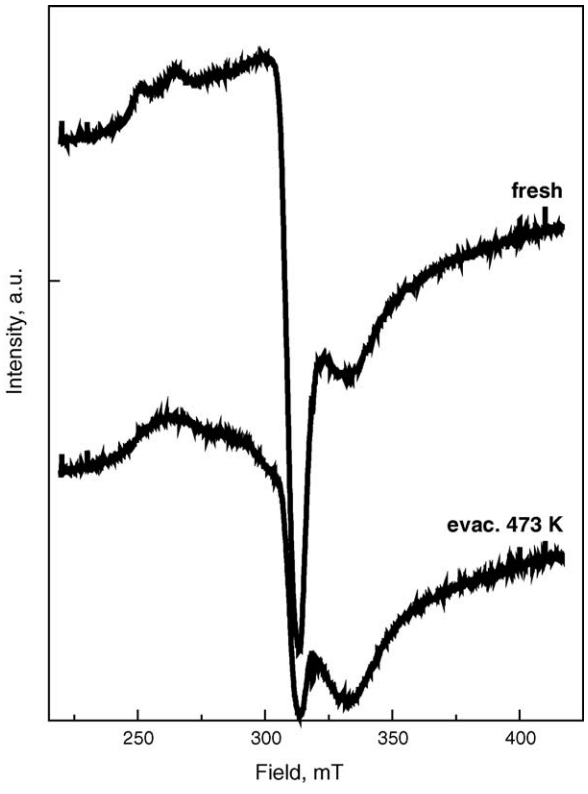

Fig. 2. ESR spectra recorded at 77 K for CuNbMCM-41-32 sample (fresh and after evacuation at 473 K) [24].

After stirring in water, both samples (CuAlMCM-41-32w and CuNbMCM-41-32w) contain copper in octahedral coordination with water molecules. In case of CuAlMCM-41-32w, this coordination is present up to the evacuation at RT. Above mentioned results indicate that the stirring in water causes the substitution of copper coordinated with oxygen for copper octahedraly coordinated with water molecules, localised in the extra framework positions. Such copper transforms to species coordinated with oxygen (type II) at more drastic conditions than those necessary for the parent materials (before stirring in water).

2.3.2. The iron containing samples

2.3.2.1. Role of texture/structure of matrix. The composition of iron containing samples is shown in Table 10. All applied procedures for incorporation of iron into micro- and mesoporous matrices did not distort the structure of the molecular sieves as evidenced from the XRD patterns shown in [21]. Only the introduction of ferroceneacetic acid (FAA) into the MCM-41 materials slightly changes the XRD patterns. The decrease in intensity as well as the broadening of XRD peaks result from FAA immobilisation [27].

Fe^{3+} ions in the zeolite system occupy the $^6S_{5/2}$ ground electronic Russel–Saunders state for high-spin d^5 ions. Therefore, the ESR spectroscopy is useful in investigation zeolites containing Fe^{3+}. The ESR parameters of Fe^{3+} depend on the local crystal field. The calcination of Fe-ZSM-5 (CVD) in O_2 at 873 K results in the ESR lines (not shown here) at $g = 6.5$, 5.8, and 4.28 [19]. According to [51–55], the lines at $g = 6.5$ and 5.8, could be assigned to isolated Fe^{3+} ions with low symmetry and that at $g = 4.28$ to tetrahedral Fe^{3+}. However, it is no agreement in the literature due to the assignment of $g = 6$ ESR signal. For instance Zhmidomirov and co-workers [56] stated

Table 10
Composition of iron micro- and mesoporous materials [19,21,27]

Sample	Si/T[a]	Fe/T[a]	Fe (wt.%)
Fe-ZSM-5 (IE)	31	0.30	1.0
Fe-ZSM-5 (CVD)	11.75	1.06	–
Fe-SiMCM-41 (TIE)	–	–	2.9
Fe-AlMCM-41 (TIE)	32	0.33	1.0
Fe(FAA)MCM-41	–	–	0.55
Fe(FAA)AlMCM-41-32	32		2.08
Fe(FAA)AlMCM-41-128	128		0.63

[a] T: Al or Nb in the framework.

that this signal originates from octahedral Fe^{3+} complex tetrahedrally distorted. Kucherov and Slinkin [53] assigned this kind of species to distorted tetrahedral Fe^{3+}. Goldfarb and co-workers [54] attributed the low field signal at $g = 6.3$ to Fe^{3+} sites with a dominating ZFS (Zero Field Splitting) interaction and an asymmetry parameter, E/D, of = 0.2. This kind of species occupies highly asymmetric sites situated at ''defect'' framework or extra framework sites. The ESR zero field splitting (ZFS) parameters D and E measure the deviation of the ion crystal field from ideal tetrahedral or octahedral symmetries and they apply to ions with more than one unpaired electron, e.g., low field Fe^{3+} and Mn^{2+}. However, the broad nature of the Fe^{3+} ESR spectra makes determining D and E difficult [57,58]. Coming back to the ESR results shown in [19], it is important to stress that there was no line at $g = 2.3$, which is characteristic of the Fe^{3+} ion in the iron oxide phase. This result indicates that the majority of the Fe^{3+} ions in Fe-ZSM-5 (CVD) are isolated in more or less distorted coordination. The ESR spectra of Fe-ZSM-5 (IE) zeolite are shown in Fig. 3. Contrarily to the case of Fe-ZSM-5 (CVD) there are not well resolved Fe^{3+} at $g = 6.5$ and 5.8. The increase of evacuation temperature to 973 K causes the appearance of a very small signal at $g = 6.23$ which is assigned in the literature [59,60] to Fe^{3+} in the coordination of the less distorted tetrahedron. A narrow ESR signal at $g = 2.003$ can originate from a coke formed from the residual template but also it can be due to Fe^{3+} octahedrally coordinated as isolated ions at cationic positions [61]. Moreover, Sachtler and co-workers [59] attributed a sharp line to superoxide ions (O_2^-) which are associated with iron ions. In addition, a broad signal described by $g = 2.0$ appears. In the literature, a broad signal ($g = \sim 2.2$) is assigned to iron-oxide phase. For example, Hagen et al. [61] observed a similar signal in H-[Fe-Al]-MFI samples and stated that it is due to aggregated hydroxide/oxide species, whereas Sachtler and co-workers [59] observed a similar ESR line over Fe_2O_3/HMFI and attributed it to iron in small Fe_2O_3 particles. It can also be attributed to the superparamagnetic iron species (like small extra framework Fe–O clusters or to tiny ferric oxide particles) [55,60,62] or ultradispersed iron oxide species with ferromagnetic behaviour [56]. This signal is better visible when the spectrum is scanned at RT (not shown here). However, the precise assignment of this kind of species requires the additional studies by UV–vis, Mössbauer, EXAFS or/and magnetic measurements.

The ESR spectra of Fe-AlMCM-41 are similar to that of Fe-ZSM-5 (IE). The same signals are registered in the low field region ($g > 3$) which are attributed to isolated Fe^{3+} ions in different coordination environments, as well as lines at $g < 3$ originating from Fe-oxo species. However, the increase of the evacuation temperature to 973 K causes the decrease of the intensity of all the ESR signals showing that Fe^{3+} species in aluminosilica mesoporous matrix are less stable than when they are located in microporous ZSM-5 zeolite [23].

Fig. 4 shows the ESR spectra of Fe-MCM-41 (TIE) material. They differ from those described above showing the domination of the signal at $g = 2.2$ and a very weak one from Fe^{3+} ($g = 4.27$, Fig. 4). These signals are visible after evacuation at 573 K but completely disappear when a higher evacuation temperature is applied (773 K). The above results allow the statement that iron is not grafted to the silicate framework as Bourlinos et al. [63] observed in Fe-planted MCM-41 samples. It is worthy of notice that all paramagnetic Fe^{3+} species disappears upon evacuation of the sample at 773 K suggesting either the reduction of Fe^{3+} to Fe^{2+}or the formation of other iron ESR silent species.

The iron species formed on the Fe-molecular sieves surfaces strongly depends on the structure of the support, the nature of

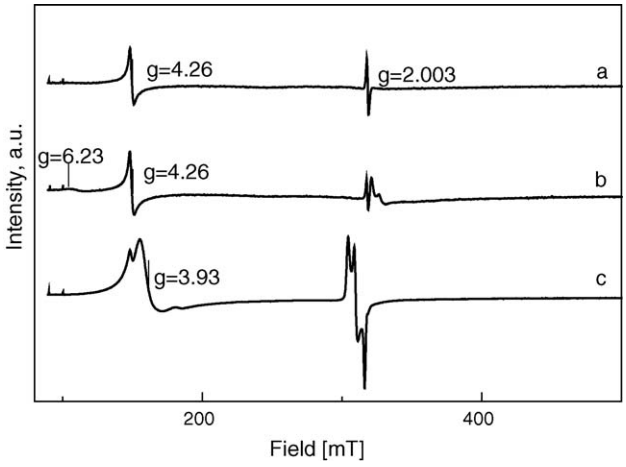

Fig. 3. ESR spectra recorded at 77 K for Fe-ZSM-5 (IE) after evacuation at 773 K, 2 h (a), 973 K, 2h (b), and adsorption 1 mbar of NO and evacuation at RT 10 min (c) [13].

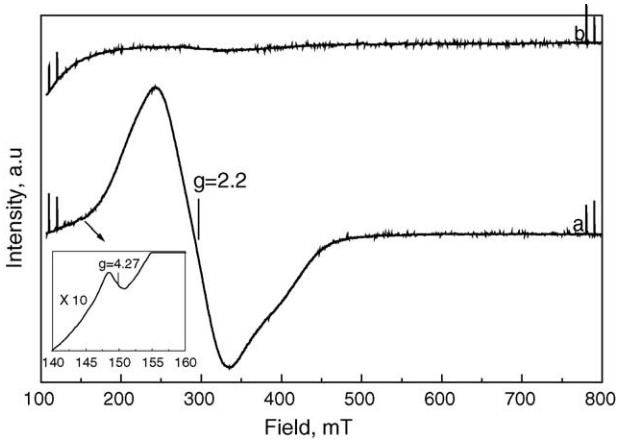

Fig. 4. ESR spectra recorded at 77 K for Fe-MCM-41 (TIE) after evacuation at 573 K, 2 h (a), and at 773 K, 2 h (b) [23].

T-atom in the framework, and the calcination temperature. Mesoporous structures are conductive to the formation of Fe-oxo species. This species is the main one observed on Fe-MCM-41(TIE) (a broad signal at $g = 2.2$) [21,23].

2.3.2.2. Iron species from FAA immobilisation in mesoporous matrices. A very important aspect of catalytic chemistry is a method of catalyst preparation, and it usually plays a key role in achievement of required properties of active species. A new method, the immobilisation of ferroceneacetic acid (FAA) on various MCM-41 mesoporous molecular sieves (containing Si or Si + Al) followed by calcinations at 773 K has been applied for the formation of iron active species [27,64]. The question arises which kind of iron species is formed after calcination of FAA immobilized materials. One could expect the presence of separate iron oxide phase in the FAA loaded samples calcined at 773 K, like it has been found in the MCM-41 molecular sieves impregnated with iron inorganic salts [23,65,66]. Meanwhile a Mössbauer spectroscopy as well as most ESR spectra did not indicate the presence of separate iron oxide phase. Such a phase can be well observed in the ESR spectrum recorded at room temperature in the shape of wide ESR signal ($g = 2.1$). As it is shown in Fig. 5, this kind of signal is only slightly visible, most for the higher iron loading (in Fe(FAA)/AlMCM-41-32).

The ESR study allows the estimation of the influence of matrix composition on the nature of iron species formed. The ESR spectra of all materials exhibit the presence of Fe^{3+} paramagnetic species characterised by a signal at $g = 4.27$ typical of Fe^{3+} tetrahedrally coordinated species [23,53]. It is accompanied by a low intensity signal at $g = 6.07$ due to the distorted Fe^{3+} tetrahedrally species [53,60] or tetrahedral distorted octahedral Fe^{3+} species [56], which is well visible only in the case of low Fe loading. The evacuation at 693 K causes the significantly increase in the intensity of the signal at $g = 4.27$ for the samples based on Al-containing matrices. This growth is more evidenced at the higher content of aluminium (Si/Al = 32). It is worthy of notice that iron species on AlMCM-41 matrices is easier reduced by CO than the other one detected on Fe(FAA)/MCM-41 (Fig. 6). Although both kinds of Fe^{3+} species give rise to the same ESR signal at $g = 4.27$ their properties are different. Therefore, one can postulate that Fe^{3+} species in cationic positions, easily reducible, dominates in the material with higher content of aluminium, Si/Al = 32 (Fe^{3+} compensate the negative charge of aluminium tetrahedra in the skeleton), but it is also present to some extent in the samples with lower Al content. However, in the matrix which does not exhibit negative charge of the skeleton (silicate MCM-41) iron cannot be located in the extra framework cationic positions but it is anchored into the walls. Therefore, this kind of iron species is not easily reduced by CO, what is documented by the ESR 4.27 signal (Fig. 6) which does not disappear after CO treatment and heating at 623 K. Iron more embedded into the MCM-41 matrix than into AlMCM-41-32 one has been also postulated on the basis of the Mössbauer study [27].

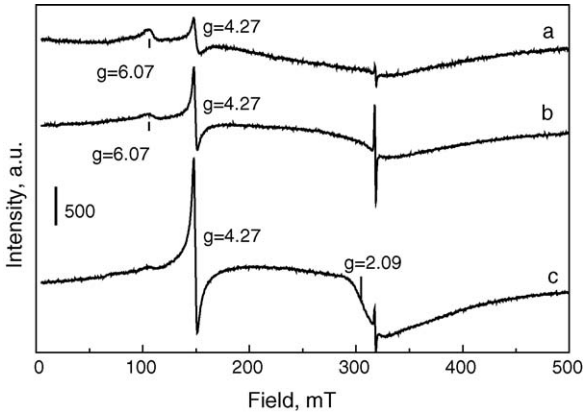

Fig. 5. ESR spectra recorded at RT after evacuation at 693 K, 2 h, for Fe(FAA)/MCM-41 (a), Fe(FAA)/AlMCM-41-128 (b), and Fe(FAA)/AlMCM-41-32 (c) [27].

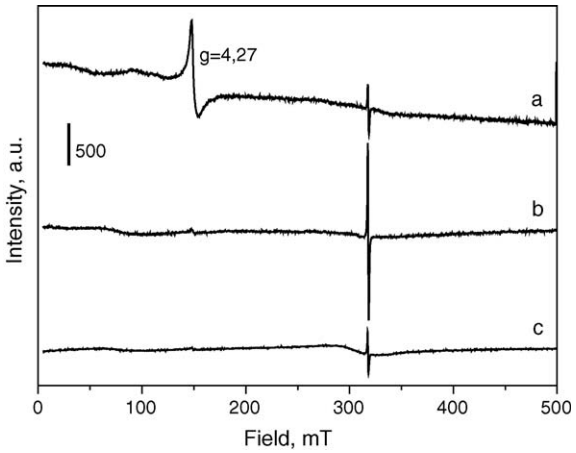

Fig. 6. ESR spectra recorded at 77 K after reduction with CO at 623 K, 7 h for Fe(FAA)/MCM-41 (a), Fe(FAA)/AlMCM-41-128 (b), and Fe(FAA)/AlMCM-41-32 (c) [27].

2.3.2.3. ESR study of Fe containing ZSM-5 and MCM-41 materials after adsorption of NO, SO_2, and 2-methylpropane (iso-butane). Nitrogen oxide is a good probe molecule for the identification of Fe^{2+} similar as Cu^{+} isolated species if its adsorption is combined with ESR measurements. Although, it is stable radical, NO in its ground state ($^2\Pi_{1/2}$) does not exhibit an ESR signal unless the degeneracy of its π orbitals is removed [67]. The signal should be observable if the orbital moment of the electron is quenched, i.e., if the degeneracy among the π orbitals is removed by its environment [68]. The electric field associated with the Fe^{2+} isolated cations might bring about such quenching of the orbital moment.

The adsorption of NO on all the samples studied gives rise to the appearance of ESR signals in the range between 300 and 350 mT and another one in the low field ($g = 3.93$) (shown for Fe-ZSM-5 (IE) Fig. 3). The latter origins from $(NO)_2$ biradicals. The lines in the 300–350 mT region are not typical of mono or biradical of NO, i.e., triplet from the hyperfine structure of N from NO or $(NO)_2$. Most probably the superposition of ESR signals from mono, biradicals of nitrogen oxide and Fe-oxo species occurs [13,23]. The presence of Fe^{2+} isolated cations (ESR-mono and biradicals of NO adsorbed on Fe^{2+}) was found in all materials studied, but their amount is negligible on Fe-

MCM-41 (TIE). The latter material exhibits the highest concentration of Fe oxide species and the lowest amount of tetrahedral coordinated Fe^{3+}.

In situ ESR study of NO-SCR was carried out for the estimation of the influence of Fe^{3+} paramagnetic species on a mechanism of SCR process [19]. After NO-SCR on Fe-ZSM-5 (CVD) at 623 K, the signals arising from distorted tetrahedral coordination decreased in the ESR spectra. On the contrary, a line at $g = 4.28$ changed insignificantly. In other words, the former species takes part in the catalytic cycle while the latter does not. Lee and Rhee [69] reported that the concentration of isolated Fe^{3+} cations in distorted tetrahedral coordination was correlated with the reactivity of the catalysts. In the same manner, the active centres seem to be mainly distorted tetrahedral Fe^{3+} species at $g = 5.8$ and 6.5 [19].

When SO_2 is present in the reaction mixture, the lines at $g = 5.8$ and 6.5 disappear completely and the line at $g = 4.28$ decreases a slightly. This provides the evidence that Fe^{3+} with distorted tetrahedral coordination are poisoned by SO_2. It implies that SO_2 plays a crucial role in reducing the active sites, which are distorted tetrahedral Fe^{3+} [19].

A signal at $g = 1.9978$ which was observed after SCR reaction of NO in the presence of SO_2 can be assigned to a hexacoordinated Fe^{3+} complex with octahedral symmetry. However, the formation of Fe^{3+} species is not probable because Kucherov et al. [70] observed the reduction of Fe^{3+} to Fe^{2+} after treating of Fe-ZSM-5 with C_3H_6 at 523 K. Hence, one can exclude the possibility of the assignment of this signal to the hexacoordinated Fe^{3+} complex with octahedral symmetry. The next possibility for the assigment of this signal at $g = 1.9978$ is the paramagnetic coke species because the colour of Fe-ZSM-5 (CVD) was changed from red-yellow to dark brown. This peak at $g = 1.9978$ was recorded after the adsorption of *iso*-butane followed by heating in vacuum at 523 and 623 K, that also caused the colour change of the sample to dark brown. Kucherov and Slinkin [53] reported that a calcination of solid-state ion-exchanged Fe-ZSM-5 with *p*-xylene sorbed at 293 K led to the formation of coke, producing a narrow ESR line with $g = 2.002$ typical of *p*-xylene cation radicals. Therefore, it is concluded that SO_2 facilitates coke formation on the surface during NO-SCR in the presence of SO_2.

2.3.3. Niobium containing samples

The compositions of Nb containing catalysts and pore volumes are given in Table 11. Various paramagnetic species could exist on niobium containing materials. If niobium is incorporated into the framework of MCM-41 mesoporous sieves, one can expect the existence of paramagnetic Nb^{4+} exhibiting 10 hyperfine lines [71–74]. It could be more than 10 lines if a defect is located on Nb–O–Nb unit due to two Nb nuclei [71]. Moreover, oxygen radical species as well as a defect hole centre are possible to be formed during heating or irradiation. First [17], it has been found the formation of oxygen radicals on the Nb(O)MCM-41-32 sample and assigned to the framework NbO^- formed as a result of the dehydroxylation (Fig. 7). A similar ESR spectrum was registered when the mesoporous molecular sieve was produced from $NbCl_5$.

Table 11
Composition and physical properties of the samples used in this work [20]

Sample[a]	Nb-source/preparation	Si/Nb	Total pore volume ($cm^3\ g^{-1}$) BJH-des
Nb(Cl)MCM-41-32	Nb(V) chloride synthesis	32	1.10
Nb(O)MCM-41-32	Nb(V) oxolate synthesis	32	1.55
Nb(O)MCM-41-16	Nb(V) oxolate synthesis	16	1.37

[a] The latest number denotes the assumed Si/Nb ratio.

NbMCM-41 mesoporous sieves dehydroxylated during the activation at 573–723 K exhibit pairs of Lewis acid–base centres as shown in [17]. The presence of both active sites was proven by FTIR measurements after NO adsorption [17,20]. $Nb–O^-$ species could play the role of Lewis base or oxidizing centre. It was evidenced from NO adsorption experiments that this species exhibits a strongly oxidizing character.

If $Nb–O^-$ plays the role of an oxidizing centre, it could exhibit an ion-radical character. The ESR observed signals are not due to the paramagnetic Nb^{4+} centre, because for such a centre one can expect 10 ESR lines with $g = 1.89$ [74]. Moreover, the oxidation state of Nb atoms in the framework of mesoporous MCM-41 was reported as Nb^{5+} due to the absence of ESR signal (Nb^{5+} exhibit diamagnetic properties) [75] and XPS measurement [26]. The evacuation at 573 K gives rise to a signal ($g = 2.031$ and 2.005) like that described in the literature for Nb_2O_5 doped TiO_2 [76], which was assigned to the oxygen species formed by photo-irradiation of Nb═O species which changed into $Nb–O^-$ one. In the experiment described by Fig. 7, the following evacuation of the sample at 723 K reveals

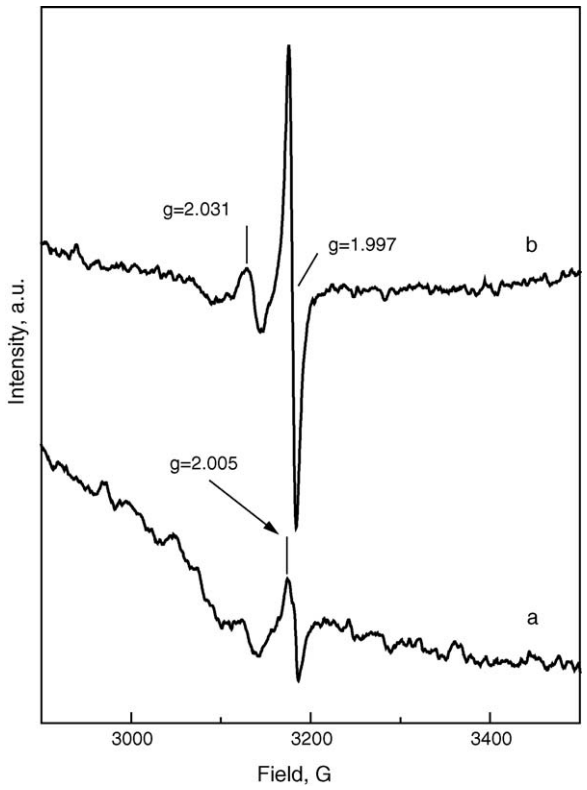

Fig. 7. ESR spectra recorded at 77 K for NbMCM-41-32, after evacuation at 573 K (a) and 723 K (b) [17].

Table 12
Composition and physical properties of the vanadium containing samples [25,26]

Sample	Si/Me assumed	Si/Me real	Surface area (m^2/g) BET	Mesopore volume (cm^3/g) BJH-des	Pore diameter (nm)
VMCM-41-32	Si/V = 32	259	1070	1.17	3.45
VMCM-41-128	Si/V = 128	1950	1090	1.17	3.31
VNbMCM-41-51	Si/Nb = 256	216	970	1.00	3.22
	Si/V = 64	272			

the arising of a sharp signal with $g = 1.997$. Such signal is characteristic for a hole centre generated by the oxygen present in the semiconductors [77] and was also described for niobium oxide evacuated at 773 K and interpreted as a hole mainly localised on an oxygen atom near a niobium atom [72,73]. One cannot exclude the origin of this sharp band from residual traces of a template [32].

The ESR spectrum of Nb(O)MCM-41-16 sample (Si/Nb = 16, i.e., a higher concentration of Nb than in the samples characterised by Si/Nb = 32) varies from those in Fig. 7. It includes the signals (not shown here) with $g = 2.0010$, 2.0049, and 2.039 attributed on the basis of [78–80] to O_2^- radical, and another one with $g = 1.987$ assigned in the literature to the lattice defects [76] formed by the desorption or dissociation of oxygen. The observed decrease of the signal intensity with O_2 introduction and heating at 723 K was caused by the readsorption of oxygen on the surface of the sample. The described behaviour can be explained by the high concentration of NbO^- species in Nb(O)MCM-41-16 which results in the easier release of oxygen than that from the sample with Si/Nb = 32 [20]. The $g_{zz} = 2.039$ of O_2^- radicals well correlates with that calculated by Che and Giamello [80] for O_2^- interacting with M^{4+} cations. Therefore, one can suppose that with a high Nb content (Si/Nb = 16), the partial reduction of Nb^{5+} to Nb^{4+} occurs under evacuation leading to the interaction with O_2^- [20].

2.3.4. Vanadium containing catalysts

All materials which are shown in Table 12 exhibit the nitrogen sorption isotherms of type IV in the IUPAC classification and well hexagonal ordered mesoporous structure of MCM-41 type and a very high specific surface area (ca. 1000 $m^2\ g^{-1}$) [25,26].

Vanadium species in VMCM-41 materials has been estimated by UV–vis and ESR spectroscopies. In this review ESR spectra are discussed (Fig. 8).

The ESR spectrum of the fresh calcined VMCM-41-32 material (Fig. 8) shows the broad signal at $g = 1.971$ which shape and g factor are similar to that described in [81] for VO^{2+} ions. The signal width indicates a high local spin concentration of vanadyl VO^{2+} ions. Such vanadyl ions are not present in the fresh calcined VMCM-41-128 exhibiting much lower vanadium content (Fig. 8b). However, evacuation at 573 K causes the reduction of V^{5+} to VO^{2+} species and the hyperfine structure of isolated VO^{2+} ions appears (Fig. 8c). The presence of V^{5+} ions in VMCM-41-128 samples was confirmed by the UV–vis study of the fresh calcined material [25]. The ESR spectra of VNbMCM-41-51 material (not shown here), in which hyperfine

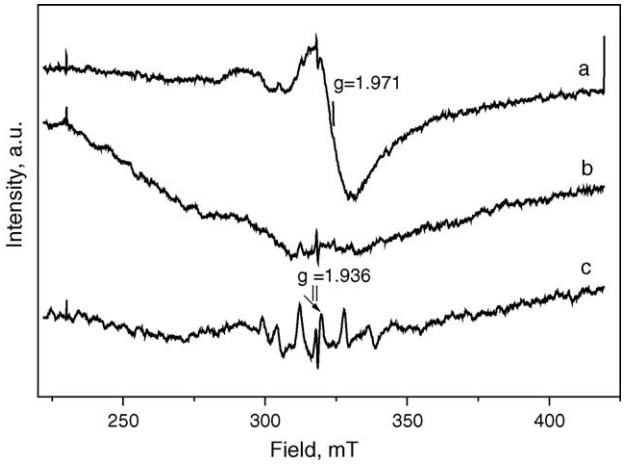

Fig. 8. ESR spectra recorded at 77 K for VMCM-41 samples: VMCM-41-32, fresh sample (a), VMCM-41-128, fresh sample (b), and VMCM-41-128 sample after evacuation at 573 K (c) [25].

structure from isolated VO^{2+} ions is not present in the fresh material, but is very well visible after evacuation at 573 K [26]. Similarly to VMCM-41-32, a broad ESR signal indicates a high local spin concentration of vanadyl VO^{2+} ions, suggesting the presence of such species on the surface of MCM-41. Moreover, the ESR spectrum of VMCM-41-32 material after evacuation at 573 K does not show well visible hyperfine structure from isolated vanadyl ions contrarily to VNbMCM-41-51 catalyst. This result indicates an influence of Nb presence on the reduction of vanadium in the MCM-41 material like it was observed for Cu, Nb-containing materials.

Table 13
Summary of transition metal states

Species	The spin Hamiltonian parameters	
	g	$A_{\|\|}$ (G)
Cu octahedrally coordinated	2.39–2.37	135–138
Cu with square pyramidal coordination	2.35–2.30	131–169
Cu four-coordinated complex with tetrahedrally distorted square symmetry	2.34	138
Cu with square planar structure	2.27–2.29	162–169
Aggregated hydroxide/oxide species	≈2.1–2.2	
Isolated Fe^{3+} in tetrahedral coordination	4.27–4.28	
Isolated Fe^{3+} in the coordination of the less distorted tetrahedron	5.8–6.5	
Isolated VO^{2+} ions with square pyramidal structure	≈1.4	191
NbO^- species	2.031 and 2.005	

3. Summary

The presented results confirmed that ESR spectroscopy is a useful tool for the study of transition metal state in zeolites and mesoporous molecular sieves. It allows not only the detection of paramagnetic cations but also the diamagnetic ones after chemisorption of paramagnetic probe molecule like NO. Moreover, the surrounding of metal as well as metal oxide species can be concluded from the ESR spectra. It has been also proved that this technique helps in the estimation of the reducibility of paramagnetic metal species and leads to the description of metal coordination on the solid surface.

The various metal species identified in modified silicate, aluminosilicate and niobosilicate micro- and mesoporous molecular sieves are presented in Table 13.

Acknowledgement

I am grateful to Prof. M. Ziolek from Adam Mickiewicz University in Poznań, Poland, for very helpful discussion of ESR results.

References

[1] J.C. Lunsford, Adv. Catal. 22 (1972) 265.
[2] C. Naccache, Y.B. Tarrit, ESR Study of Adsorbed Species on Catalyst Surface, Institut De Recherches Sur La Catalyse (CNRS) (1974).
[3] R.A. Schoonheydt, Catal. Rev. Sci. Eng. 35 (1) (1993) 129.
[4] Z. Sojka, Catal. Rev. Sci. Eng. 37 (3) (1995) 461.
[5] K. Dyrek, M. Che, Chem. Rev. 97 (1997) 305.
[6] M. Hartmann, L. Kevan, Chem. Rev. 99 (1999) 635.
[7] Z. Sojka, M. Che, C.R. Acad. Sci. Paris Ser IIc 3 (2000) 163.
[8] Z. Sojka, M. Che, Appl. Magn. Reson. 20 (2001) 433.
[9] A. Brückner, Catal. Rev. Sci. Eng. 45 (1) (2003) 97.
[10] G. Grubert, M.J. Hudson, R.W. Joyner, M. Stockenhuber, J. Catal. 196 (2000) 126.
[11] M. Stockenhuber, M.J. Hudson, R.W. Joyner, J. Phys. Chem. B 104 (2000) 3370.
[12] M. Stockenhuber, R.W. Joyner, J.M. Dixon, M.J. Hudson, G. Grubert, Microporous Mesoporous Mater. 44–45 (2001) 367.
[13] P. Decyk, M. Trejda, M. Ziolek, C.R. Chimie 8 (2005) 635.
[14] M. Ziolek, I. Sobczak, P. Decyk, I. Nowak, Pol. J. Environ. Stud. 6 (1997) 47.
[15] M. Ziolek, I. Sobczak, P. Decyk, I. Nowak, Stud. Surf. Sci. Catal. 125 (1999) 633.
[16] M. Ziolek, I. Nowak, I. Sobczak, A. Lewandowska, P. Decyk, J. Kujawa, Stud. Surf. Sci. Catal. 129 (2000) 813.
[17] M. Ziolek, I. Sobczak, I. Nowak, P. Decyk, A. Lewandowska, J. Kujawa, Microporous Mesoporous Mater. 35–36 (2000) 195.
[18] M. Ziolek, I. Sobczak, I. Nowak, P. Decyk, J. Stoch, Stud. Surf. Sci. Catal. 135 (2001), 07-O-04.
[19] P. Decyk, D.K. Kim, S.I. Woo, J. Catal. 203 (2001) 369.
[20] M. Ziolek, I. Sobczak, A. Lewandowska, I. Nowak, P. Decyk, M. Renn, B. Jankowska, Catal. Today 70 (2001) 169.
[21] P. Decyk, M. Trejda, A. Lewandowska, M. Ziolek, Pol. J. Environ. Stud. 10 (2001) 50.
[22] I. Sobczak, P. Decyk, M. Ziolek, M. Daturi, J.C. Lavalley, L. Kevan, A.M. Prakash, J. Catal. 207 (2002) 101.
[23] P. Decyk, M. Trejda, M. Ziolek, A. Lewandowska, Stud. Surf. Sci. Catal. 142 (2002) 1785.
[24] I. Sobczak, M. Ziolek, M. Renn, P. Decyk, I. Nowak, M. Daturi, J.C. Lavalley, Microporous Mesoporous Mater. 74 (2004) 23.
[25] M. Ziolek, I. Nowak, B. Kilos, I. Sobczak, P. Decyk, M. Trejda, J.C. Volta, J. Phys. Chem. Solids 65 (2004) 571.
[26] B. Kilos, J.C. Volta, I. Nowak, P. Decyk, M. Ziolek, Stud. Surf. Sci. Catal. 154 (2004) 848.
[27] M. Trejda, K. Lazar, P. Decyk, Z. Fojud, S. Jurga, M. Ziolek, Stud. Surf. Sci. Catal. 158 (2005) 829.
[28] M. Ziolek, I. Nowak, Zeolites 18 (1997) 356.
[29] E. Giamello, D. Murphy, G. Magnacca, C. Morterra, Y. Shioya, T. Nomura, M. Anpo, J. Catal. 136 (1992) 510.
[30] S.C. Larsen, A.W. Aylor, A.T. Bell, J.A. Reimer, J. Phys. Chem. 98 (1994) 11533.
[31] J.-S. Yu, L. Kevan, J. Phys. Chem. 98 (1994) 12436.
[32] Z. Sojka, M. Che, E. Giamello, J. Phys. Chem. B 101 (1997) 4831.
[33] Z. Sojka, Appl. Magn. Reson. 18 (2000) 71.
[34] A. Pöppl, M. Hartmann, Stud. Surf. Sci. Catal. 142 (2002) 375.
[35] A.V. Kucherov, A.A. Slinkin, Zeolites 6 (1986) 175.
[36] J. Varga, J.B. Nagy, J. Halasz, J. Kiricsi, J. Mol. Struct. 410–411 (1997) 149.
[37] J. Soria, A.A. Martinez-Arias, A. Martinez-Chaparro, J.C. Conesa, Z. Schay, J. Catal. 190 (2000) 352.
[38] M.H. Groothaert, K. Pierloot, A. Delabie, R.A. Schoonheydt, PCCP 5 (2003) 2135.
[39] J.-S. Yu, M.C. Chang, C.-H. Kwak, Proc. Inorg. Chem. Symp. 2 (1994) 20.
[40] J.L.G. Fierro, Stud. Surf. Sci. Catal. 57 (1990) 67.
[41] B. Wichterlova, J. Dedecek, Z. Sobalik, A. Vondrova, K. Klier, J. Catal. 169 (1997) 194.
[42] J. Dedecek, B. Wichterlova, J. Phys. Chem. 98 (1994) 5721.
[43] J. Dedecek, Z. Sobalik, Z. Tvaruzkova, D. Kaucky, B. Wichterlova, J. Phys. Chem. 99 (1994) 16327.
[44] B. Gil, J. Datka, S. Witkowski, Z. Sojka, E. Brocławik, Stud. Surf. Sci. Catal. 130 (2000) 3249.
[45] A.V. Kucherov, A.A. Slinkin, D.A. Kondratev, T.W. Bondarenko, A.M. Rubinstein, Kh. M. Minacher Zeolites 5 (1985) 320.
[46] A.V. Kucherov, A.N. Shigapov, A.A. Ivanov, M. Shelef, J. Catal. 186 (1999) 334.
[47] C. Henriques, M.F. Ribeiro, C. Abreu, D.M. Murphy, F. Poignant, J. Saussey, J.C. Lavalley, Appl. Catal. B 16 (1998) 79.
[48] S.K. Hoffmann, J. Goslar, J. Solid State Chem. 44 (1982) 343.
[49] J. Goslar, A.B. Więckowski, J. Solid State Chem. 56 (1985) 101.
[50] T. Munoz Jr., A.M. Prakash, L. Kevan, K.J. Balkus Jr., J. Phys. Chem. B 102 (1998) 1379.
[51] B. Wichterlova, Zeolites 8 (1981) 181.
[52] J. Varga, J. Halasz, D. Horwath, D. Mehn, J.B. Nagy, G. Schobel, I. Kiricsi, Stud. Surf. Sci. Catal. 116 (1998) 367.
[53] A.V. Kucherov, A.A. Slinkin, Zeolites 8 (1988) 110.
[54] D. Arieli, D.E.W. Vaughan, K.G. Strohmaier, H. Thoman, M. Bernardo, D. Goldfarb, Magn. Reson. Chem. 37 (1999) S43.
[55] G. Berlier, G. Spoto, S. Bordiga, G. Ricchiardi, P. Fisicaro, A. Zecchina, I. Rossetti, E. Selli, L. Forni, E. Giamello, C. Lamberti, J. Catal. 208 (2002) 64.
[56] A.M. Volodin, W.I. Sobolev, G.M. Zhidomirov, Kinet. Catal. 39 (1998) 844.
[57] B. Sutter, T. Wasowicz, T. Howard, R. Hossner, D.W. Ming, Soil Sci. Soc. Am. J. 66 (2002) 1359.
[58] D.E. De Vos, B.M. Veckhuysen, T. Bein, J. Am. Chem. Soc. 118 (1996) 9615.
[59] H.-Y. Chen, El-M. El-Malki, X. Wang, R.A. van Santen, W.M.H. Sachtler, J. Mol. Catal. A 162 (2000) 159.
[60] S. Bordiga, R. Buzzoni, F. Geobaldo, C. Lamberti, E. Giamello, A. Zecchina, G. Leofanti, G. Petrini, G. Tozzola, G. Vlaic, J. Catal. 158 (1996) 486.
[61] A. Hagen, F. Roessner, I. Weingart, B. Spliethoff, Zeolites 15 (1995) 270.
[62] D.H. Lin, G. Coudurier, J.C. Vedrine, Stud. Surf. Catal. 49 (1989) 1431.
[63] A.B. Bourlinos, M.A. Karakassides, D. Petridis, J. Phys. Chem. 104 (2000) 4375.
[64] M. Trejda, M. Ziolek, Catal. Today 101 (2005) 109.
[65] P. Selvam, S.E. Dapurkar, S.K. Badamali, M. Murugasan, H. Kuwano, Catal. Today 68 (2001) 69.

[66] S. Liu, W. Wang, P. van der Voort, P. Cool, E.F. Vansant, M. Jiang, J. Magn. Magn. Mater. 280 (2004) 31.
[67] P.H. Kasai, R.M. Gaura, J. Phys. Chem. 86 (1982) 4257.
[68] P.H. Kasai, R.J. Bishop Jr., J. Am. Chem. Soc. 94 (1972) 5560.
[69] H.-T. Lee, H.-K. Rhee, Catal. Lett. 61 (1999) 173.
[70] A.V. Kucherov, C.N. Montreuil, T.N. Kucherova, M. Schelef, Catal. Lett. 56 (1998) 173.
[71] A.M. Prakash, L. Kevan, J. Am. Chem. Soc. 120 (1998) 13148.
[72] D. de, A.B. Filho, D.W. Franco, P.P.A. Filho, O.L. Alves, J. Mater. Sci. 33 (1998) 2607.
[73] Y.M. Kim, D.E. Reardon, P.J. Bray, J. Chem. Phys. 48 (1968) 3396.
[74] M. Sugantha, G.V. Subbo Rao, J. Solid State Chem. 111 (1994) 33.
[75] L. Zhang, J.Y. Ying, AIChE J. 43 (1997) 2793.
[76] H. Kokusen, S. Matsuhara, Y. Nishino, S. Hasegawa, K. Kubono, Catal. Today 28 (1996) 191.
[77] D.L. Griscom, in: D.R. Uchlman, N.J. Kreidl (Eds.), Glass: Science and Technology, Harcourt Brace Jovanovich, Arizona, 1990, p. 151.
[78] M. Che, A.J. Tench, Adv. Catal. 31 (1982) 77.
[79] M. Che, A.J. Tench, Adv. Catal. 32 (1983) 1.
[80] M. Che, E. Giamelo, Stud. Surf. Sci. Catal. 57 (1990) 265.
[81] Z. Luan, J. Xu, H. He, J. Klinowski, L. Kevan, J. Phys. Chem. 100 (1996) 19595.